Unlocking the Potential of A-Site Ca Doped $LaCo_{0.2}Fe_{0.8}O_{3-\delta}$: A Redox-Stable Cathode Material Enabling High Current Density in Direct CO_2 Electrolysis

AUTHOR NAMES: Haixia Li[1], Wanhua Wang[1], Lucun Wang[2], Min Wang[2], Ka-Young Park[1], Taehee Lee[1], Andreas Heyden[3], Dong Ding[2] and Fanglin Chen[1*]*

AUTHOR ADDRESS:

[1] Department of Mechanical Engineering, University of South Carolina, Columbia, SC, 29208, USA

[2] Energy & Environmental Science and Technology, Idaho National Laboratory, Idaho Falls, ID, 83401, USA

[3] Department of Chemical Engineering, University of South Carolina, Columbia, SC, 29201, USA

ABSTRACT: Massive carbon dioxide (CO_2) emission from recent human industrialization has affected the global ecosystem and raised great concern for environmental sustainability. Solid oxide electrolysis cell (SOEC) is a promising energy conversion device capable of efficiently converting CO_2 into valuable chemicals using renewable energy sources. However, Sr-containing cathode materials face the challenge of Sr carbonation during CO_2 electrolysis, which greatly affects the energy conversion efficiency and long-term stability. Thus, A site Ca doped $La_{1-x}Ca_xCo_{0.2}Fe_{0.8}O_{3-\delta}$ ($0.2 \leq x \leq 0.6$) oxides are developed for direct CO_2 conversion to carbon monoxide (CO) in an intermediate-temperature SOEC (IT-SOEC). With a polarization resistance as low as 0.18 Ω cm^2 in pure CO_2 atmosphere, a remarkable current density of 2.24 A cm^{-2} was achieved at 1.5 V with $La_{0.6}Ca_{0.4}Co_{0.2}Fe_{0.8}O_{3-\delta}$

(LCCF64) as the cathode in $La_{0.8}Sr_{0.2}Ga_{0.83}Mg_{0.17}O_{3-\delta}$ (LSGM) electrolyte (300 μm) supported electrolysis cells using $La_{0.6}Sr_{0.4}Co_{0.2}Fe_{0.8}O_{3-\delta}$ (LSCF) as the air electrode at 800 °C. Furthermore, symmetrical cells with LCCF64 as the electrodes also show promising electrolysis performance of 1.78 A cm^{-2} at 1.5 V at 800 °C. In addition, stable cell performance has been achieved on direct CO_2 electrolysis at an applied constant current of 0.5 A cm^{-2} at 800 °C. The easily removable carbonate intermediate produced during direct CO_2 electrolysis makes LCCF64 a promising regenerable cathode. The outstanding electrocatalytic performance of the LCCF64 cathode is ascribed to the highly active and stable metal/perovskite interfaces resulted from the *in situ* exsolved Co/CoFe nanoparticles, and the additional oxygen vacancies originated from the $Ca_2Fe_2O_5$ phase, synergistically providing active sites for CO_2 adsorption and electrolysis. This study offers a novel approach to design catalysts with high performance for direct CO_2 electrolysis.

KEYWORDS: Solid oxide electrolysis cell (SOEC), perovskite, direct CO_2 electrolysis, CO_2 absorption, cathode, symmetrical cell.

1. INTRODUCTION

The extensive combustion of fossil fuels for human activities is an inevitable process that results in significant amounts of CO_2 emissions. Excessive CO_2 emissions have led to the greenhouse effect, climate change, and ecosystem degradation, posing severe challenges to human society.[1] It is, therefore, crucial to develop efficient methods for converting superfluous CO_2 into useful chemicals to mitigate CO_2 concentration in the atmosphere. CO_2 electrolysis, also known as CO_2 reduction reaction (CO_2RR), has been identified as a promising approach for converting CO_2 to valuable chemical CO with high efficiency via solid oxide electrolysis cells (SOECs).[2] Typically, a SOEC consists

of an anode (air electrode), a cathode (CO_2 electrode), and an electrolyte that separates the two electrode chambers. As one of the core components in this configuration, the cathode is where CO_2 conversion takes place, involving CO_2 adsorption/dissociation, CO desorption, and oxygen vacancy migration, etc., and thus the properties of the cathode material are incredibly vital to the CO_2 reduction reaction.[3]

To date, various materials have been investigated as cathode materials for CO_2 electrolysis in SOECs. Notably, Ni-based cathodes have demonstrated the most promising performance due to their excellent catalytic activities and high electrical conductivity.[4] However, Ni is susceptible to deactivation due to redox instability and carbon deposition, and it's necessary to supply a protective reducing gas (e.g., H_2, CO) during the CO_2 electrolysis to prevent Ni from being re-oxidized by CO_2. However, adding a protective reducing gas to the CO_2 stream increases energy cost and complicates the electrolysis procedures.[5] Alternatively, perovskite-related oxides including single perovskites, double perovskites, and Ruddlesden–Popper type layered perovskites have attracted considerable research attention due to their high mixed ionic/electronic conductivity, good redox stability, good coking resistance, etc., and have been extensively studied as SOEC cathode for direct CO_2 electrolysis. For example, $La_{0.75}Sr_{0.25}Cr_{0.5}Mn_{0.5}O_{3-\delta}$ (LSCM),[6] (La,Sr)(Fe,Ti)O_3,[7–9] $Sr_2Fe_{1.5}Mo_{0.5}O_{6-\delta}$,[10,11] and (La,Sr)$FeO_{4+\delta}$,[12,13] et al. have been investigated as cathode materials for CO_2 electrolysis. However, those cathode materials still show insufficient electrochemical performance compared to the Ni-based cathodes. Considering the process of CO_2 electrolysis, CO_2 would first need to gain electrons from the applied current and be reduced to CO and O^{2-} on the cathode side (eq. 1); subsequently, O^{2-} permeates through the porous cathode and the dense electrolyte and then releases electrons to form O_2 on the porous anode (eq. 2).[14]

$$2CO_2 + 2e^- = 2CO + O^{2-} \quad (1)$$

$$2O^{2-} = O_2 + 4\ e^- \quad (2)$$

It can been seen that oxygen vacancy in the perovskite material is vital for O^{2-} migration. Hence, designing cathode materials with high oxygen vacancy or high oxygen ion conductivity is critical to improve CO_2 electrolysis.

In the past few years, there has been growing interest in B site Co-Fe-based perovskite materials as potential electrodes for solid oxide cells (SOCs) or oxygen permeation membranes due to their excellent electronic and oxygen ion conductivity, as well as their good electrocatalytic activity.[15-17] In particular, $La_{1-x}A_xCo_{0.2}Fe_{0.8}O_{3-\delta}$ (where A = Sr/Ba/Ca and x = 0.2, 0.4, 0.6) has shown great promise as an oxygen-permeable material at intermediate temperatures.[18-20] Among them, $La_{0.6}Sr_{0.4}Co_{0.2}Fe_{0.8}O_{3-\delta}$ has demonstrated excellent catalytic activity for oxygen evolution/oxygen reduction reaction and outstanding performance as an air electrode material for SOCs.[15] Furthermore, the presence of transition metals Co and Fe at the B-site of the perovskite structure enables their facile participation under reducing atmospheres, resulting in the formation of alloy nanoparticles embedded on the perovskite backbone, creating numerous nanoparticle/backbone interfaces. These interfaces serve as highly active sites for the CO_2 reduction reaction, thereby substantially enhancing the catalytic activity of the CO_2 electrode.[21,22] Therefore, applying Co-Fe-based perovskite as a cathode for direct CO_2 electrolysis holds the promise to achieve high-performance SOECs. For instance, $La_{0.4}Sr_{0.6}Co_{0.2}Fe_{0.7}Nb_{0.1}O_{3-\delta}$ perovskite oxide has been investigated as the cathode for CO_2RR in a symmetrical SOEC. CoFe alloy nanoparticle was formed as a catalyst during CO_2 electrolysis and the cell performance is better than that of LSCM (180 mA cm^{-2} @ overpotential of 1.62 V at 800 °C),[6,21] or $SrTiO_3$ (140 mA cm^{-2} @ applied voltage of 1.6 V at 800 °C).[7] Feng et al. employed

$La_{0.6}Sr_{0.4}Co_{0.2}Fe_{0.8}O_{3-\delta}$ as the cathode in a SOEC for CO_2 electrolysis, achieving a current density of 2.03 A cm^{-2} at 1.6 V at 800 °C. However, they observed a significant degradation in cell performance within the first 6 hours, which was attributed to the formation of $SrCO_3$ particles on the $La_{0.6}Sr_{0.4}Co_{0.2}Fe_{0.8}O_{3-\delta}$ (LSCF) cathode surface.[16] When reviewing the Sr-containing perovskite cathode materials, the issue of $SrCO_3$ formation is not unique to Co-Fe-based cathodes. Hou et al. observed a similar problem when $La_{0.5}Sr_{0.5}FeO_{3-\delta}$ was used for CO_2 electrolysis, resulting in a significant amount of $SrCO_3$ formation that negatively affected the materials' conductivity and blocked active sites, leading to poor cell performance stability.[23] Similarly, Hu et al. reported that excessive $SrCO_3$ formation on the surface of $Sr_2Fe_{1.5-x}Ni_xMo_{0.5}O_{6-\delta}$ ($x = 0$, 0.05, 0.1, 0.2) perovskites hindered the charge transfer and oxygen species diffusion, leading to reduced cell performance.[14] Therefore, cathode materials containing Sr have the issue of Sr carbonation, and it is crucial to find a substitution for Sr when developing promising cathode materials for CO_2 electrolysis.[24]

Previous studies have indicated that perovskite oxide materials having Ca doped on the A-site are less susceptible to carbonation when exposed to CO_2 containing atmosphere than those Sr or Ba doped materials.[18,25,26] For example, Song et al. investigated $La_{0.6}A_{0.4}FeO_{3-\delta}$ (A = Ca, Sr, and Ba) as oxygen ion conductor materials, and they found that $La_{0.6}Ca_{0.4}FeO_{3-\delta}$ are less vulnerable towards carbonation upon exposure to CO_2 when compared with Sr/Ba doped ones.[18] Similarly, when Ca-doped $LaFeO_3$ perovskite was studied as a cathode material in solid oxide fuel cells, both the experimental and DFT calculation results confirmed that $La_{0.6}Ca_{0.4}FeO_{3-\delta}$ exhibited better CO_2 tolerance than the materials without Ca.[25] Apart from the better CO_2 tolerance of Ca doped material, from the perspective of perovskite structure stability, the use of Ca may be more advantageous than Sr or Ba due to the fact that the ionic radius of Ca^{2+} (1.0 Å) is

closely matched to that of La^{3+} (1.03 Å) than Sr^{2+} (1.18 Å) or Ba^{2+} (1.35 Å), which may reduce the likelihood of Sr/Ba segregation from the lattice.[27] For instance, the crystal structure and the electrical conductivity of $La_{1-x}Ca_xFe_{0.8}Ni_{0.2}O_{3-\delta}$ ($0 \leq x \leq 0.9$) were systematically investigated by Rojo et al., and they found that rather than A site segregation, a secondary brownmillerite-type ($Ca_2Fe_2O_5$) structure phase would form with higher Ca content ($x \geq 0.5$), which could improve the ionic conductivity of the materials.[28]

A-site Ca-doped perovskites have been studied as cathodes for CO_2 electrolysis.[26,29-31] For instance, Ca-doped $La_{0.6}A_{0.4}Fe_{0.8}Ni_{0.2}O_3$ exhibited superior electrochemical performance compared to Sr/Ba-doped materials due to its appropriate conductivity, suitable oxygen vacancy concentration, and high catalytic activity for CO_2RR.[26] Additionally, $La_{0.6}Ca_{0.4}Fe_{0.8}Ni_{0.2}O_{3-\delta}$ was examined as a symmetrical SOEC electrode for CO_2 electrolysis, achieving a current density of 1.41 A cm^{-2} at 2.0 V with direct CO_2 electrolysis at 800 °C. Interestingly, it has been demonstrated that the $La_{0.6}Ca_{0.4}Fe_{0.8}Ni_{0.2}O_{3-\delta}$ electrodes could be easily restored through air treatment after CO_2 electrolysis operation to prevent carbonate formation.[30] Given the promising results of A-site Ca-doped perovskite cathodes, it is reasonable to expect that Ca doping in Co-Fe-based perovskites could enhance their catalytic activity for CO_2 electrolysis by generating oxygen vacancies and Co/CoFe alloy nanoparticles as catalysts.

In this work, Ca doped-$LaCo_{0.2}Fe_{0.8}O_{3-\delta}$ ($La_{1-x}Ca_xCo_{0.2}Fe_{0.8}O_{3-\delta}$ (x=0.2-0.6)) cathode materials, abbreviated as LCxCF (x=0.2-0.6), are synthesized and studied as cathodes for SOECs using a sol-gel combustion method. The influence of Ca doping on various aspects, including structural characteristics, surface morphology, redox behavior, CO_2 adsorption, electrical properties, and polarization resistance, are evaluated in detail. Furthermore, single cells with the cell configuration of LCxCF//LSGM//LSCF are

fabricated, and their electrochemical performance are evaluated in the temperature range of 650 to 800 °C. Meanwhile, the reversibility of the cell after the long-term operation has been assessed by refreshing the cathode with a simple air treatment. The results of this study are expected to provide valuable guidance for developing sustainable cathode materials for highly efficient CO_2 electrolysis in intermediate-temperature SOECs.

2. EXPERIMENTAL SECTION

2.1. Materials Synthesis. $La_{1-x}Ca_xCo_{0.2}Fe_{0.8}O_{3-\delta}$ (x=0.2-0.6) powders were synthesized using a sol-gel method.[32] Specifically, a stoichiometric amount of the precursor chemicals of $La(NO_3)_2 \cdot 6H_2O$, $Ca(NO_3)_3 \cdot 4H_2O$, $Co(NO_3)_2 \cdot 6H_2O$, and $Fe(NO_3)_3 \cdot 9H_2O$ were dissolved in distilled water to form a transparent solution. Glycine and citric acid were then added to the solution as the chelating agent, with a molar ratio of metal cations to citric acid to glycine at 1:1.5:2. The solution was heated at 80 °C with constant stirring until a gel was formed. The gel was then further heated on a hot plate at 400 °C until self-ignition occurred. Afterward, the precursor powder was collected, pulverized, and calcined at 1100 °C for 5 hours in the air to obtain LCxCF powders. The notations LCCF82, LCCF73, LCCF64, LCCF55, and LCCF46 correspond to $La_{1-x}Ca_xCo_{0.2}Fe_{0.8}O_{3-\delta}$, where x takes the values of 0.2, 0.3, 0.4, 0.5, and 0.6, respectively. LSCF air electrode powder was purchased from Fuel Cell Materials.

2.2 Characterization. The crystalline phases of the synthesized LCxCF powders as well as those heat-treated under different atmospheres were examined by powder X-ray diffraction (XRD) (Rigaku MiniFlex II) with CuKα radiation (λ=0.15415nm). The microstructure of the LCxCF powders and electrolyte-supported single cells was characterized using a field emission scanning electron microscope (SEM, Zeiss Ultra Plus FESEM).

Thermal gravimetric analysis (TGA) was employed to determine the weight change of LCxCF powders under different gas atmospheres. The TGA experiments were carried out using an STA 449 F3 thermal analyzer (NETZSCH, Germany) from 30 to 900 °C at a heating rate of 5 °C/min with a gas flow rate of 50 mL/min using either air or 4% H_2/N_2.

Carbon dioxide temperature-programmed desorption (CO_2-TPD) experiments were conducted using an Auto Chem II 2920 workstation (Micromeritics instrument corporation, USA). Prior to the experiments, LCxCF powders were pretreated in helium at 300 °C for 1 h to remove surface-adsorbed impurities. Subsequently, the samples were cooled down to 50 °C and saturated in CO_2 for 2 h. Thermal desorption was carried out by heating the powder (150 mg) in 5% CO_2-He (50 mL min^{-1}) at a heating rate of 10 °C/min from 50 to 900 °C. CO_2 desorption signels were recorded using a thermal conductivity detector for subsequent analysis.

The surface oxygen profiles of LCCF82, LCCF64, and LCCF46 pristine powders and those heat-treated in 50% CO/CO_2 were analyzed using X-ray photoelectron spectroscopy (XPS) with a PHI VersaProbe III spectrometer. The binding energy was calibrated using C 1s with a value of 284.8 eV. The O1s peaks were fitted using Shirley baseline with the peak fitting parameters of GL(30) within CasaXPS.

Dense LCxCF bar samples with dimensions of approximately 34 mm × 6.9 mm × 0.7 mm were fabricated by uniaxially pressing the corresponding powders with 4% (PVB) binder under 7 MPa pressure for 1 min. The resulting samples were then sintered in air at 1220 °C for 5 hours. The electrical conductivity of LCxCF bar samples was determined using the DC four-probe method with a Keithley 2001 multimeter in air or CO_2 at temperatures ranging from 450 to 850 °C, respectively.

2.3 Cell Fabrication and Electrochemical Performance Testing. Dense LSGM

electrolyte pellets with a thickness of approximately 300 μm were prepared via the uniaxially pressing of commercial LSGM powders (Fuelcellmaterials, USA) using a stainless-steel die. The pellets were sintered at 1450 °C for 6 h. Electrode powders and V006 binder in a weight ratio of 1:1.5 were grounded in an agate mortar to obtain the electrode ink. The LCxCF cathode and LSCF anode ink were brushed on either sides of the LSGM pellets with an active area of 0.33 cm^2, respectively. Following the drying of the electrode ink, the single cells with the cell configuration of LCxCF//LSGM//LSCF were calcined at 1000 °C for 2 h in air. After heat-treatment, the thickness of the cathode and anode is ~30 μm and ~20 μm, respectively. Gold paste was applied on the top of the anode and cathode to attach silver mesh as the current collector and calcinated at 800 °C for 1 h to remove the organic substance in the gold paste. Finally, the as-fabricated single cells were sealed on an aluminum tube using ceramic sealant (Ceramabond 552) for the cell electrochemical performance measurement.

The cathode polarization resistance (Rp) was evaluated through symmetrical cells consisting of LCxCF ink on both sides of the LSGM electrolyte, with an active electrode area of 0.33 cm^2. The symmetrical cell's fabrication process is the same as that of the single cell. Sliver mesh was utilized as a current collector on the electrode surface, which was affixed using gold paste.

Current density-voltage (I-V) curves of the SOECs were obtained over the temperature range of 650-800 °C, utilizing a Versa STAT 3-400 electrochemical workstation. In addition, electrochemical impedance spectra (EIS) were acquired at OCV for both single and symmetrical cells with a frequency range of 10^6 to 0.01 Hz and an AC amplitude of 10 mV.

For the evaluation of Faraday efficiency, different current densities ranging from 0.3 to

1.5 A cm^{-2} were applied to the single electrolysis cell for 45 min, and the composition of outlet gas was analysized using a gas chromatography (GC) (Agilent 7890A, USA). The values of CO concentration in the last three measurements were recorded for Faraday efficiency calculation. The flow rate of CO_2 on the cathode side was 30 ml min^{-1}, and the anode was exposed to air.

3. RESULTS AND DISCUSSION

3.1. Crystal Structure. X-ray diffraction (XRD) patterns shown in Figure 1(a) depict the pristine $La_{1-x}Ca_xCo_{0.2}Fe_{0.8}O_{3-\delta}$ (x=0.2-0.6) powders after calcination at 1100 °C for 5 h in the air. The main phase observed from the powders of the five different compositions is an orthorhombic perovskite structure with the space group Pbnm (62) (PDF# 97-015-3875), consistent with the structure of undoped $LaFeO_3$.[33] LCCF82 and LCCF73 are pure phases without any impurities. However, as the Ca content increases, the powders exhibit an increasing evident of a secondary phase. Specifically, LCCF64, LCCF55, and LCCF46 show a secondary phase that can be identified as a brownmillerite $Ca_2Fe_2O_5$ phase (PDF#97-008-8986). Figure 1(d) provides an enlarged view of Figure 1(a) with 2θ from 28° to 36°, depicting the $Ca_2Fe_2O_5$ phase in greater detail. The substitution of La^{3+} (1.36 Å) with smaller Ca^{2+} (1.34 Å), as well as the reduction in mean ionic radius at the B-site (from Fe^{3+} (0.645 Å) to Fe^{4+} (0.585 Å) and from Co^{2+} (0.745 Å) to Co^{3+} (0.61 Å)) due to charge compensation cause a shrinkage in the crystal lattice, which contributes to the formation of a secondary $Ca_2Fe_2O_5$ phase.[28]

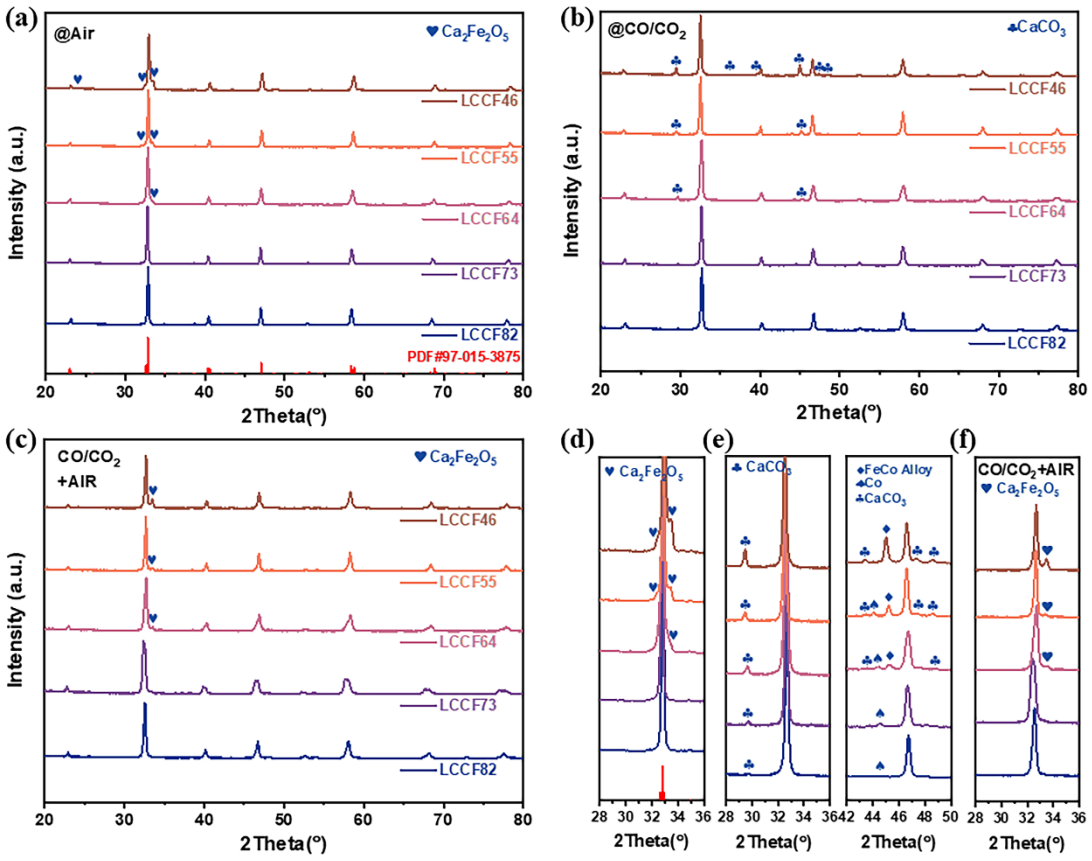

Figure 1. X-ray diffraction patterns of LCxCF (x=0.2-0.6) powder (a) calcinated at 1100 °C in air for 5h, (b) treated in 50% CO/CO_2 for 10 h at 800 °C, and (c) re-calcination of 50% CO/CO_2 treated LCxCF (x=0.2-0.6) powder in air for 10 h; (d) is the enlarged view of (a) between 28-36°; (e) is the enlarged view of (b) between 28-36 ° and 42-50°; (f) is the enlarged view of (c) between 28-36 °.

To assess the stability of the LCxCF materials in the CO_2 atmosphere, they were exposed to CO_2 at 800 °C for 10 h. As illustrated in Figure 2(a), the perovskite structure of LCxCF materials remains unaltered, and no impurities were detected, suggesting that the LCxCF materials have good compatibility with CO_2. However, during CO_2 electrolysis, the cathode material would go through a CO/CO_2 mixture atmosphere due to the production of CO. Thus, the XRD patterns of the LCxCF materials after being heat-treated at 800 °C for 10 h in a 50% CO/CO_2 mixture gas are presented in Figure 1(b) and Figure 1(e) (the enlarged view of 2θ in 28-36° and 42-50° in Figure 1(b)), clearly revealing the appearance of a new phase corresponding to $CaCO_3$ (PDF# 97-016-9915) and a rise in intensity with increasing Ca content. Meanwhile, the extra peaks

located at 44.5° and 45.2° matched the metal Co (PDF#97-004-4989) and CoFe alloy (PDF#97-010-2383), respectively. The peak intensity of metal Co increases with Ca content rising from 0.2 to 0.5, whereas the CoFe alloy emerges when Ca content increases from 0.4 to 0.6. Although Co and Fe ions are partially exsolved from the parent phase and $CaCO_3$ formed in the CO/CO_2 mixture gas, the main crystal structure of LCxCF remains stable. Interestingly, when the CO/CO_2 mixture gas treated powders were subsequently calcined in air at 800 °C for 10 hours, as shown in Figure 1(c) and Figure 1(f) (the enlarged view of 2θ in 28-36 degree in Figure 1(c)), the $CaCO_3$ phase totally vanished while the peak intensity of $Ca_2Fe_2O_5$ phase exhibited a slight decrease when compared to the pristine phase of LCxCF (Figure 1(d)), indicating the issue of Ca carbonation can be mitigated by a simple heat treatment in air.

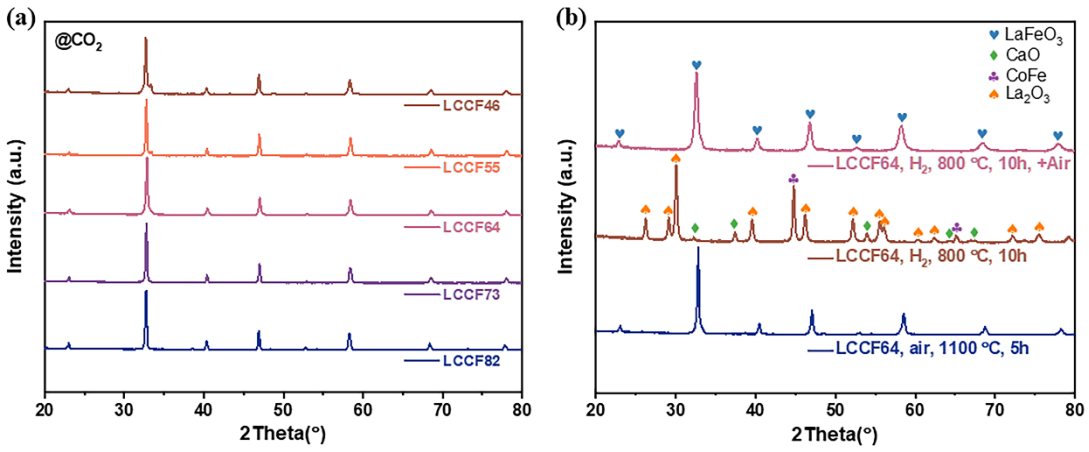

Figure 2. X-ray diffraction patterns of LCxCF (x=0.2-0.6) powder (a) treated in pure CO_2 for 10 h at 800 °C, and (b) Pristine LCCF64 powder treated in dry H_2 and then heat-treated in air at 800 °C for 10 h.

The above XRD analysis has revealed that the formation of $CaCO_3$ occurs exclusively when LCxCF is subjected to a CO/CO_2 reducing atmosphere, possibly attributed to the segregation of CaO in such a condition. This phenomenon was investigated by subjecting pristine LCCF64 powder to dry H_2 at 800°C for 10 hours, resulting in the decomposition of the perovskite structure into La_2O_3, CaO, and CoFe alloy, as depicted

in Figure 2(b). Notably, CaO, known for its affinity towards CO_2, exhibits heightened reactivity and subsequently generates $CaCO_3$,[34] as represented by eq. 3,

$$CaO(s) + CO_2(g) \rightleftharpoons CaCO_3 \qquad (3)$$

Remarkably, even after deep reduction and subsequent decomposition of LCCF64, the perovskite phase can be fully restored through heat treatment at 800°C for 10 hours in an air environment, demonstrating its exceptional redox reversibility. Thus, in the presence of a CO/CO_2 mixture gas, decomposition of LCCF64 has been mitigated due to the oxidizing nature of CO_2 within the atmosphere.

3.2 Surface Morphology Analysis. XRD analysis in the prior section showed that secondary phase $Ca_2Fe_2O_5$ was observed in the pristine LCxCF materials with the increase in Ca content, and $CaCO_3$ along with Co/CoFe alloy phase were detected in the LCxCF samples exposed to a 50% CO/CO_2 atmosphere. Therefore, the morphology of the LCxCF powders in different atmospheres was characterized using a scanning electron microscope. Figure 3(a-e) shows the LCxCF pristine powders calcinated in air at 1100 °C for 5 h, and a porous microstructure was observed for all five LCxCF samples. However, LCCF82 and LCCF73 had a clear surface and grain boundary, while the blur grain boundary was observed with the Ca content from 0.4 to 0.6, and LCCF64 shows an apparent secondary phase with different morphology, indicating that the secondary phase observed in XRD would change the morphology of LCxCF materials. Moreover, with the increase of Ca content, the grain size increased correspondingly, which was contributed by the function of CaO as a sintering aid.[35] After treating the LCxCF powders in a 50% CO/CO_2 mixture at 800 °C for 10 h, as shown in Figure 3(f-j) and the enlargement of the rectangle in red (Figure 3(k-o)), the surface became coarse with exsolved nanoparticles. The size and number of nanoparticles increased with the increase in Ca content, which was consistent with the XRD analysis. Obviously, the

exsolved nanoparticles on the LCCF64 sample were distributed most homogeneously, while the aggregation of larger nanoparticles could be observed on LCCF55 and LCCF46 samples, which may hinder the catalytic activity of catalysts.[36]

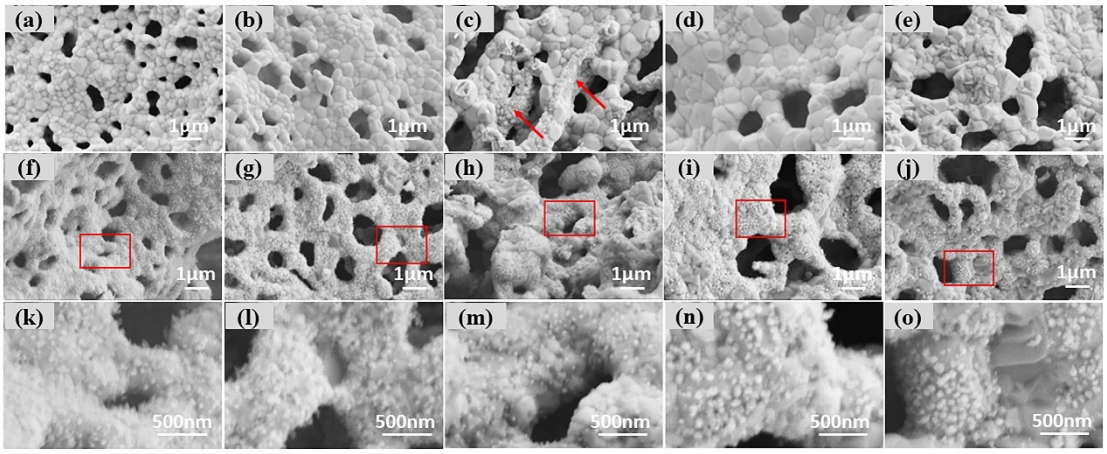

Figure 3. SEM images of the LCxCF (x=0.2-0.6) powders calcined in air at 1100 °C for 5h (a-e), and LCxCF (x=0.2-0.6) powder treated in 50% CO/CO_2 for 10 h at 800 °C (f-j); (k-o) is the enlarge of the red rectangle in (f-j), respectively.

3.3 Redox Stability Evaluation. It is widely recognized that the presence of oxygen vacancies in cathode materials plays a pivotal role in enhancing CO_2 electrolysis by creating active sites for nonpolar CO_2 adsorption. Moreover, the chemical stability of cathode materials offers the potential for achieving stable cell performance.[22,37] Therefore, TGA was employed to estimate the redox stability of LCxCF materials by monitoring the weight changes at elevated temperatures in different atmosphere.

Initially, TGA measurements were conducted in air to evaluate the behavior of lattice oxygen at elevated temperatures ranging from 30 to 900 °C. The TGA curves were recorded and depicted in Figure 4(a). The results indicate that LCxCF materials experience a primary stage of weight loss from 80 to 240 °C, which may be attributed to the loss of adsorbed water on the sample surface.[22] As the temperature increases, the weight continuously decreases and sharply drops at approximately 750 °C, which is consistent with most ABO_3 perovskites, owing to the oxygen hopping and escaping at high temperatures.[38]

In order to evaluate the stability and redox reversibility of the LCxCF cathode material during CO_2 electrolysis, TGA measurements were conducted in a gas atmosphere containing 4% H_2/N_2 to simulate the reducing environment from the CO/CO_2 mixture produced during the electrolysis. The TGA curves show apparent two-stage weight losses for LCxCF materials as presented in Figure 4(b), where a gradual weight loss below 375 °C is attributed to the desorption of moisture on the sample surface. As the temperature increases over 675 °C, the weight of the LCxCF powders experiences a sharp drop followed by a continuous decrease, indicating oxygen vacancy formation due to the lattice oxygen loss caused by the elevated temperature and the reduction of Co and Fe oxides to Co/FeCo metallic phase in the reducing atmosphere.[39,40] The higher content of Ca^{2+} replacing La^{3+} leads to a larger weight loss due to charge compensation, with LCxCF showing weight losses of 2.39%, 3.43%, 4.69%, 5.29%, and 6.89%, respectively.

After cooling down the LCxCF powders in 4% H_2/N_2 to 30 °C, the testing atmosphere was switched to air, and the same measurement process was carried out again. As shown in Figure 4(b), the short dot line showed that the weight of LCxCF powders almost regained after the ramping up in the air. For example, LCCF64 went through 4.69% weight losses when ramping up in 4% H_2/N_2 to 900 °C, and then it gained a 4.14% weight when ramping up in air. However, the weight gained was less than the weight lost. For one reason, the adsorbed water vaporized during the first ramping-up process in the 4% H_2/N_2, while no adsorbed water can lose in the second ramping-up process in air because the powders have no chance to contact ambient air. Secondly, as shown in Figure 4(a), LCxCF powders would have weight loss at elevated temperatures. Overall, the TGA analysis proves that the LCxCF materials are redox reversible, consisting with the XRD analysis, which is a vital property of the cathode material for

CO_2 electrolysis.

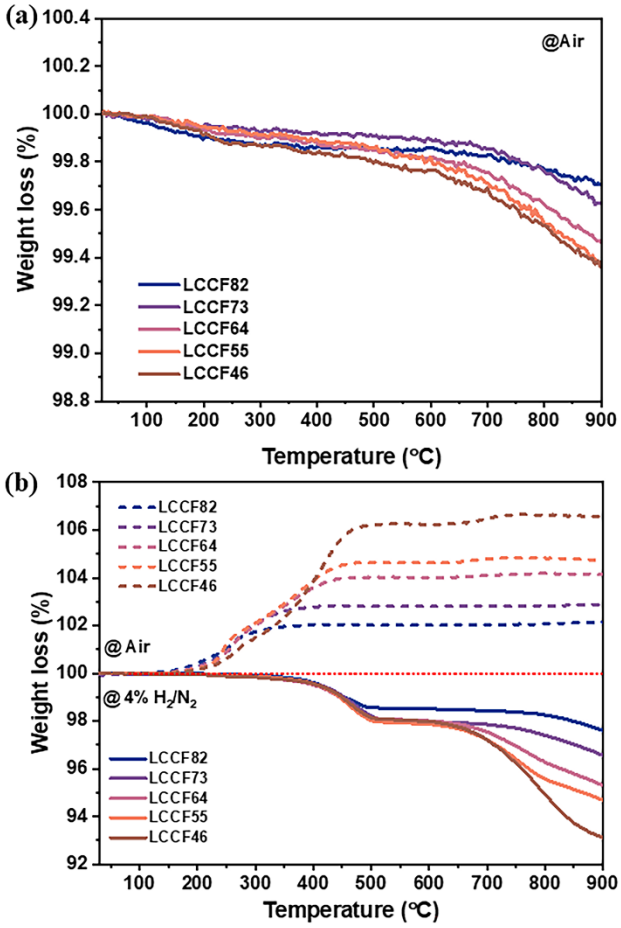

Figure 4. (a) Weight loss of LCxCF (x=0.2-0.6) powders in the air from 30 to 900 °C; (b) Redox stability evaluation of the LCxCF (x=0.2-0.6) powders by running the TGA program in a 4% H_2/N_2 flow to record the weight losing (solid lines), and then re-run the program to record the wight gaining (short dot line) of the powders by switching the flow from 4% H_2/N_2 to Air when the furnace cool down to room temperature. Note: before re-run the program, the weight of samples were re-calculated by subtracted the weight lost in the first step.

3.4 CO_2 Adsorption Property and Surface Oxygen States Analysis. The adsorption of CO_2 on the catalyst surface is a crucial step in the electro-reduction process of CO_2.[41] Thus, CO_2 temperature desorption (CO_2-TPD) measurements were performed, and Figure 5(a) illustrates the CO_2-TPD profiles of LCxCF materials. Usually, the desorption signal below 200 °C corresponds to the CO_2 physical adsorption, while the peak above 400 °C is related to the chemical adsorption.[42] And the higher desorption signal intensity represents the stronger CO_2 adsorption ability on the surface of

materials. The TPD curves of LCCF82 and LCCF73 show two peaks at the temperature range between 300 and 900 °C, which can be assigned to chemical adsorption. The first small peak is centered at ~400 °C, and the second broad peak is centered at 900 °C and 800 °C for LCCF82 and LCCF73, respectively. According to previous reports, the peak at ~400 °C may be derived from the formation of the $La_2O_2CO_3$ carbonate due to the higher amount of La at the A site.[43] Meanwhile, LCCF64, LCCF55, and LCCF46 show one broad peak starting at ~310 °C and centering at ~700 °C at the same temperature range (300-900 °C). Among them, LCCF64 exhibits the highest signal peak, suggesting that LCCF64 may possess the highest CO_2 adsorption capacity due to the lower amount of $Ca_2Fe_2O_5$ phases that were observed from XRD and SEM analysis shown in the previous section, because the $Ca_2Fe_2O_5$ phase was reported as an oxide containing large amounts of oxygen vacancy.[29] However, the desorption peak decreases even though the $Ca_2Fe_2O_5$ phase keeps increasing in LCCF55 and LCCF46, which may be due to the decreasing surface area caused by the increase in the grain size,[36] as shown in the SEM images in Figure 3(a-e).

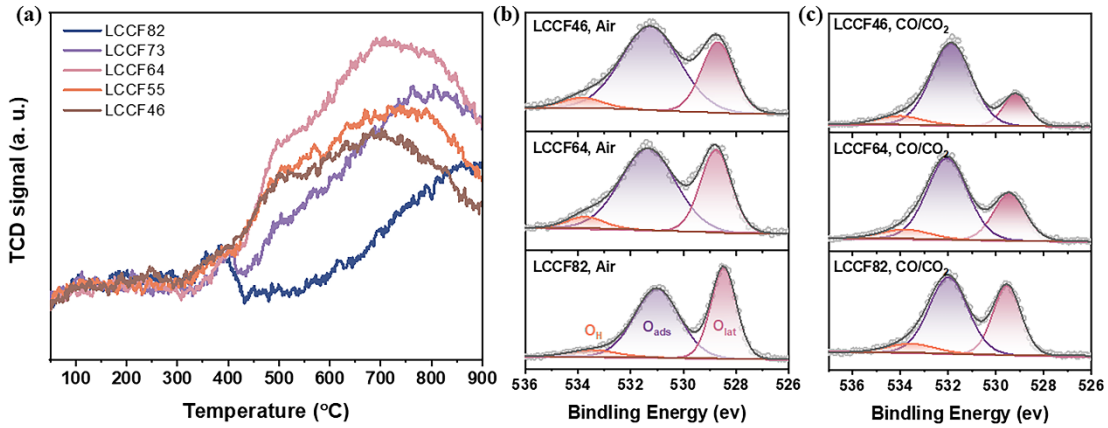

Figure 5. (a) CO_2-TPD profiles of LCxCF (x=0.2-0.6); XPS-O1s spectra of the LCxCF (x=0.2, 0.4, 0.6) powders (b) calcined in air and (c) treated in 50% CO/CO_2 atmosphere, respectively.

Since CO_2 adsorption is intimately associated with oxygen vacancies,[34] X-ray photoelectron spectroscopy (XPS) was used to reveal the surface oxygen states of LCCF82, LCCF64, and LCCF46 powders. In anticipation of exposure to a CO/CO_2 environment during CO_2 reduction, the pristine cathode powders were treated in a 50% CO/CO_2 atmosphere at 800 °C for 10 hours before the XPS measurement. The XPS-O1s spectra of untreated and CO/CO_2 mixture gas-treated powders are depicted in Figure 5(b) & Figure 5(c), respectively. XPS-O1s spectra for all the samples could be de-convoluted into three peaks. For the untreated powders, the XPS peak at lower energy (~528.6 eV) represents the lattice oxygen ion (O_{lat}) within the perovskite, and the peak at (~531.2 eV) corresponds to adsorption oxygen ions (O_{ads}), including hydroxides and carbonates.[9] Besides, a peak at ~533.7 eV means the oxygen in molecular water that adsorbed on the surface (O_H).[16,44] The percentage of lattice oxygen, adsorption oxygen, and surface adsorbed water are shown in the Table 1. As the Ca content increased, the percentage of lattice oxygen decreased, while the percentage of adsorbed oxygen increased, accounting for the formation of $Ca_2Fe_2O_5$ with Ca content increasing, leading to more oxygen vacancies, and thus promoting oxygen adsorption. For the samples treated in a CO/CO_2 mixture gas, the exsolution of Co or CoFe metal nanoparticles results in the formation of oxygen vacancy and thus increased adsorption of oxygen, as evidenced by the higher percentage of adsorbed oxygen in the XPS spectrum than the untreated powders (Figure 5(b)).

Table 1. The percentage of O_{lat}, O_{ads}, and O_H in LCCF82, LCCF64, and LCCF46 samples treated in different atmospheres

	Air			**50% CO/CO_2**		
Samples	**O_{lat} (%)**	**O_{ads} (%)**	**O_H (%)**	**O_{lat} (%)**	**O_{ads} (%)**	**O_H (%)**
LCCF82	40.55	53.95	5.50	36.78	55.24	7.98

LCCF64	34.32	60.16	5.52	28.61	63.06	8.33
LCCF46	30.39	64.20	5.41	17.97	73.63	8.40

Combining the TPD and XPS analysis, it can be seen that the substitution of La with Ca could promote the formation of oxygen vacancies, thereby increasing adsorbed oxygen. Moreover, the exsolution of Co or CoFe metal nanoparticles in the CO/CO_2 atmosphere further enhances adsorbed oxygen. Therefore, LCxCF materials show different CO_2 adsorption capacities according to the Ca content, and the CO_2 adsorption ability is associated with the oxygen vacancy and the surface area of the materials.[36]

3.5 Electrical Conductivity. The electrical conductivity of the LCxCF materials was measured using a DC four-probe method under air or CO_2 atmosphere with temperatures ranging from 450 °C to 850 °C. Figure 6(a) shows the conductivity in air. The conductivity of LCCF82 and LCCF73 increased with increasing temperature, consistent with p-type conductor behavior with a small polaron hopping mechanism.[45] However, as the Ca content increased, the conductivity of LCCF64, LCCF55, and LCCF46 initially increased up to a specific temperature and then decreased as the temperature rose to 850 °C. This phenomenon may be attributed to the presence of the $Ca_2Fe_2O_5$ phase, as reported in the XRD section. $Ca_2Fe_2O_5$ exhibits hole-type electronic conduction due to oxygen interstitials in the structure at lower temperatures, while a phase transition takes place at ~600 °C, resulting in a lower level of oxygen and thus lower electrical conductivity at higher temperatures.[46] Moreover, the conductivity of LCxCF materials increased with increasing Ca content and reached a maximum when x=0.4, accounting for the increasing formation of oxygen vacancies created by charge compensation due to a higher amount of divalent alkaline-earth Ca ion substitution for La.[18] However, the conductivity of LCCF55 and LCCF46 gradually decreased, which

may be attributed to the increased amount of $Ca_2Fe_2O_5$, which exhibits very low conductivity compared with the LCxCF perovskite structure.[47]

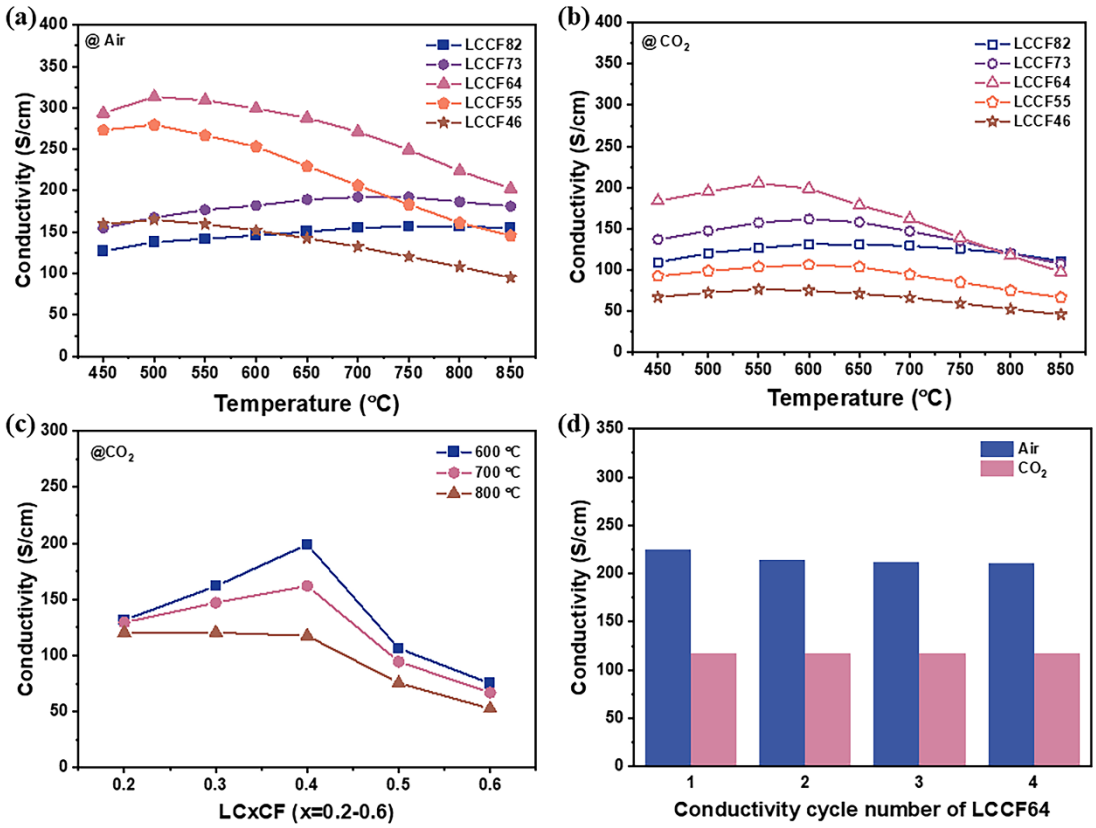

Figure 6. Electrical conductivity for LCxCF (x=0.2-0.6) in (a) air and (b) pure CO_2 from 450 to 850 °C; (c) Electrical conductivity for LCxCF (x=0.2-0.6) in pure CO_2 at 600 °C, 700 °C and 800 °C; (d) Electrical conductivity of LCCF64 with atmosphere cycling between air and pure CO_2 at 800 °C.

The conductive properties of LCxCF materials were found to be slightly lower in CO_2 due to its lower oxygen partial pressure, as shown in Figure 6(b). To better understand the relationship between the conductivity, Ca content, and temperature in a CO_2 atmosphere, the conductivity of LCxCF materials at 600 °C, 700 °C, and 800 °C was presented in Figure 6(c). The figure demonstrates that the conductivity of LCxCF decreased as the temperature increased from 600 to 800 °C, primarily due to the promotion of lattice oxygen loss at higher temperatures,[32] particularly for LCCF64 materials. In addition, the conductivity gradually increased with an increase in Ca content from x=0.2 to x=0.4 and then dropped sharply when x=0.5 and x=0.6, indicating

that the secondary phase $Ca_2Fe_2O_5$ has a significantly negative impact on the electrical conductivity. Moreover, the conductivity of LCCF64 was evaluated for four cycles in air and CO_2 to assess its reversibility in different atmospheres. Specifically, after obtaining the conductivity in air, the atmosphere was changed to CO_2, and the conductivity was measured, which was defined as one cycle. Figure 6(d) indicates that the conductivity of LCCF64 is almost reversible between air and CO_2, suggesting that LCCF64 exhibits good structural stability and compatibility with CO_2.[48]

3.6 Polarization Resistance. To evaluate the electrocatalytic activity of LCxCF materials, symmetrical cells (LCxCF//LSGM//LCxCF) were fabricated to determine the area-specific interfacial polarization resistance (Rp) through impedance analysis in air or pure CO_2 atmosphere at temperatures ranging from 650 to 800 °C. The EIS plots at different temperatures for five compositions are shown in Figure S1, where the first intercept of the impedance arc on the X-axis (Z') represents the ohmic resistance normalized to zero. The distance between the second and first intercept indicates the R_p, which is associated with charge transfer through the interface of the electrolyte and electrode, dissociative adsorption, and species transfer at the triple phase boundaries and gas diffusion process.[31] Lower R_p values usually suggest higher electrocatalytic activity. The R_p decreases with increasing temperature for all five compositions in air and pure CO_2, implying that high temperature can activate the polarization processes and improve the electrocatalytic activity of the LCxCF cathodes.[5] At 800 °C in air and CO_2 atmosphere, the R_p initially decreases and then increases with increasing Ca content. The values of polarization resistances are shown in Figure 7(a), and LCCF64 exhibits the lowest R_p in air and CO_2, corresponding to the highest electrocatalytic activity among LCxCF. The activation energy (Ea) of LCxCF materials in CO_2 is calculated from the slopes of the Arrhenius plots, as shown in Figure 7(b), which is

close to the Ea from other CO_2RR catalysts.[31,49] The LCCF64 exhibits the lowest activation energy in the CO_2 at 650-800 °C, suggesting that the LCCF64 cathode possesses the most favorable electrode properties for CO_2 electrolysis, such as gas adsorption, dissociation, and diffusion.[50]

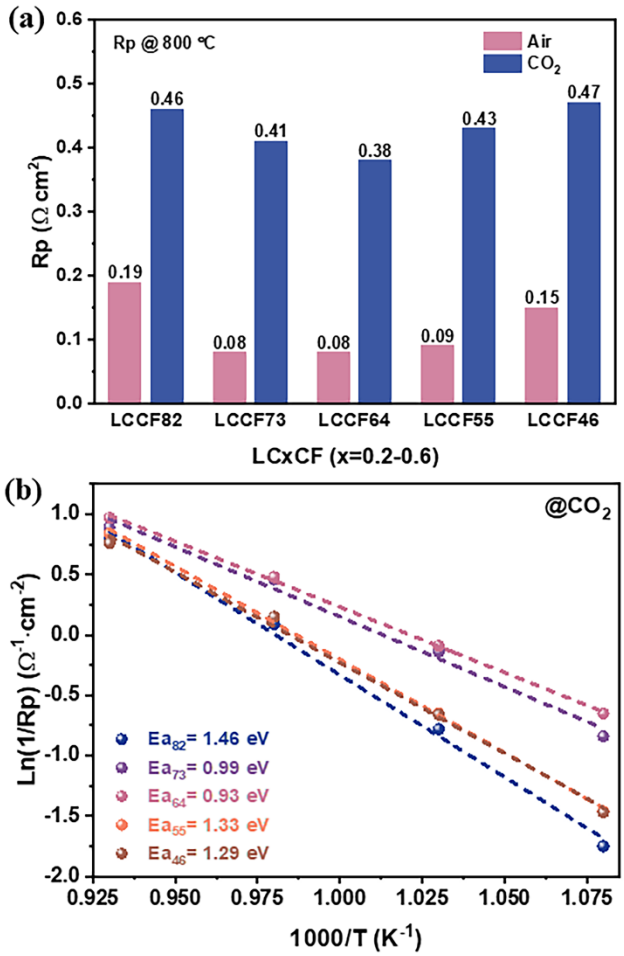

Figure 7. (a) Polarization resistance of LCxCF (x=0.2-0.6) in air and pure CO_2 at 800 °C; (b) Arrhenius plots of the R_p values of LCxCF (x=0.2-0.6) in CO_2.

3.7 Electrochemical Performance of CO_2 Electrolysis. The electrocatalytic performance of single cells with LCxCF materials as cathodes was systemically investigated. Typical I-V curves and EIS plots of the direct CO_2 electrolysis at 650-800 °C are shown in Figure S2 & Figure 8(c), and Figure S3 & Figure 8(d), respectively. For clearly comparing the cell performance, the current density of five cells at 1.5V and the ohmic resistance (R_{Ohmic}), as well as R_p of the single cells, are presented in Figure

8(a) & Figure 8(b), respectively. The results showed that the current density initially increased and then decreased with increasing Ca content, achieving 1.84, 2.01, 2.24, 1.89, and 1.43 A cm^{-2} for LCxCF under the applied voltage of 1.5 V, respectively. Meanwhile, R_{Ohmic} for five cells in Figure 8(b) is similar thanks to the same thickness of LSGM electrolyte and the excellent electrolyte-electrode connection. However, R_p for five single cells is 0.55, 0.26, 0.18, 0.41, and 0.48 Ω cm^2, respectively. Considering that the same electrolyte and anode materials were used for the five single cells, the change of R_p in the single cells could directly reflect the electrocatalytic performance of LCxCF cathode. The trend of the R_p change with different Ca content is similar to the R_p from the symmetrical cells, suggesting that the R_p obtained from the symmetrical cells is well correlated with the performance when applied as the cathode in SOECs.[49]

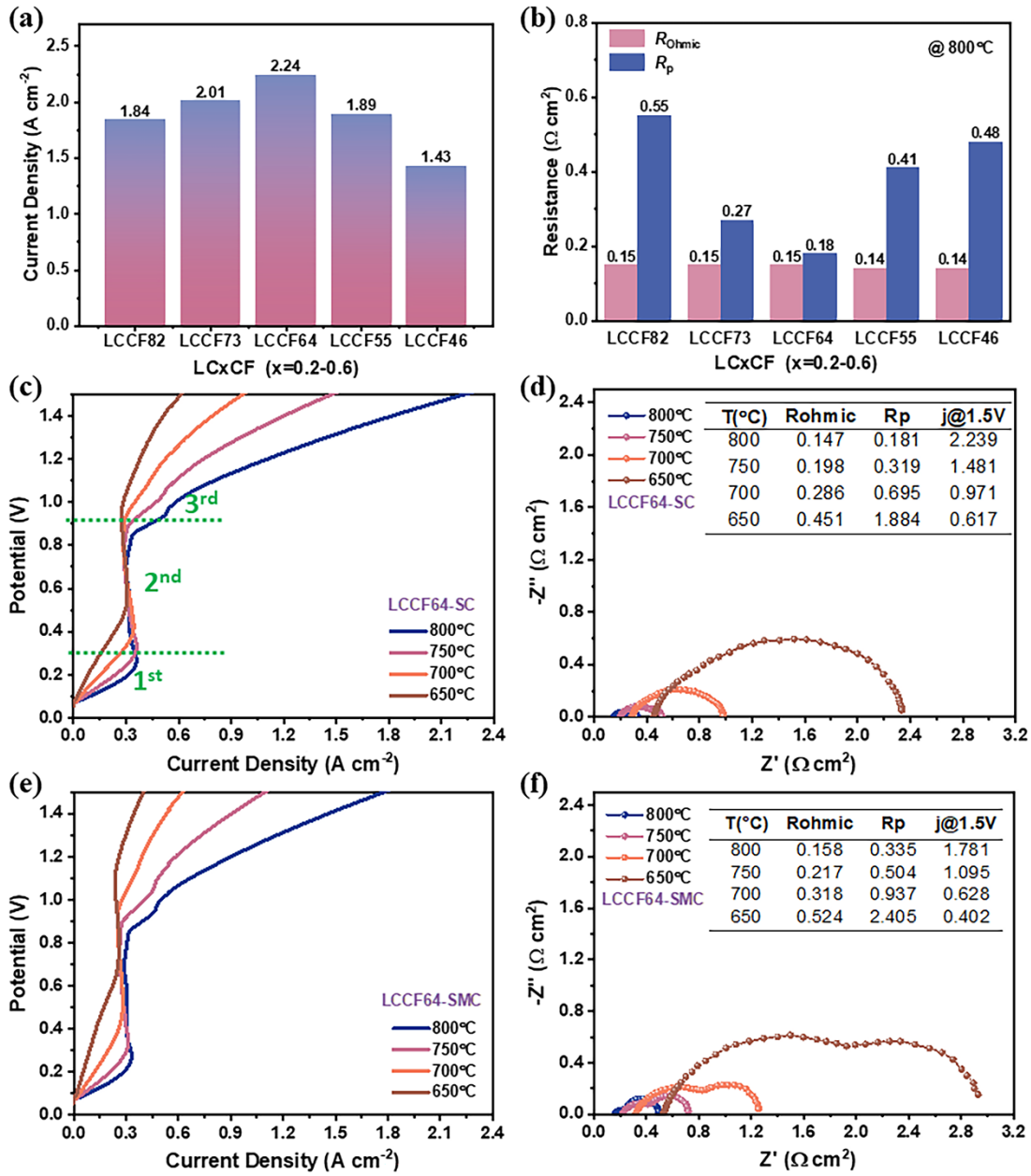

Figure 8. (a) Current density at 1.5 V and (b) the R_{Ohmic} & R_p of the single cells with LCxCF as cathode at 800 °C; (c) I-V curves and (d) Nyquist plots of the single cell (SC) with LCCF64 as cathode; (e) I-V curves and (f) Nyquist plots of the symmetrical cell (SMC) with LCCF64 as cathode and anode.

I-V curves and EIS plots of single cells with LCCF64 as the cathode are shown in Figure 8(c) and Figure 8(d), respectively. The open circuit voltage (OCV) is about 0.06 - 0.08 V in the temperature range of 650-800 °C, which is determined by the difference in oxygen partial pressure between the cathode (pure CO_2) and anode (ambient air). This is consistent with other reports on pure CO_2 electrolysis.[4,51] The I-V curve can be

divided into three regions. In the first region (1st), the current density increases as the applied voltage goes from OCV to 0.2 V due to the pumping process of oxygen gas and the net oxygen ion flux from the cathode to the anode. The oxygen may come from sealing leakage or CO_2 feeding.[51,52] The increase in current density is also attributed to the reduction of Fe^{4+}/Fe^{3+} and Co^{3+}/Co^{2+} because of the transition metal Fe and Co in the cathode composition.[53] The current density reaches a plateau at around 0.2 V and then to the second region (2nd), where the current density no longer increases with increasing the applied cell voltage, indicating the cell has reached a reaction equilibrium, but the voltage is not yet high enough to start CO_2 electrolysis. In the third region (3rd), the current density increases exponentially when the applied voltage is over 0.8 V, indicating the occurrence of CO_2 electrolysis.[21] At 1.5 V, the current density of single cells with LCCF64 cathode reaches 2.24, 1.48, 0.97, and 0.61 A cm^{-2} at 800, 750, 700, and 650 °C, respectively. R_{Ohmic} and R_p values at 800 °C in Figure 8(d) are found to be 0.14 Ω cm^2 and 0.18 Ω cm^2, respectively. When compared with previously reported cathodes for CO_2 electrolysis, LCCF64 demonstrates much lower R_p values at 800 °C, e.g., $La_{0.6}Ca_{0.4}Fe_{0.8}Ni_{0.2}O_3$ (0.737 Ω cm^2), $La_{0.6}Ba_{0.4}Fe_{0.8}Ni_{0.2}O_3$ (2.124 Ω cm^2), $La_{0.6}Sr_{0.4}Fe_{0.8}Ni_{0.2}O_3$ (1.432 Ω cm^2), [26] $La_{0.6}Sr_{0.4}FeO_3$ (1.31 Ω cm^2),[54] and $La_{0.6}Sr_{0.4}Fe_{0.95}Mo_{0.05}O_3$ (5.8 Ω cm^2).[55]

Furthermore, the performance of CO_2 electrolysis from symmetrical cells with the cell configuration of LCCF64//LSGM//LCCF64 was also evaluated. From the I-V curves in Figure 8(e), the current densities of the LCCF64 symmetrical cells at 800, 750, 700, and 650 °C are 1.78, 1.09, 0.62, and 0.40 A cm^{-2} under the applied voltage of 1.5 V, respectively. The R_p is 0.33 Ω cm^2 at 800 °C (Figure 8(f)), which is higher than the R_p of single cells (0.18 Ω cm^2 at 800 °C), indicating that the catalytic activity to oxygen evolution reaction using LCCF64 as the anode is inferior to the state-of-art LSCF anode.

However, LCCF64 symmetrical cells for CO_2 electrolysis in this work exhibits higher current density (1.78 A cm^{-2}) at 1.5V at 800 °C than symmetrical cells using other electrodes such as $La_{0.4}Sr_{0.6}Co_{0.2}Fe_{0.7}Nb_{0.1}O_{3-\delta}$ (0.442 A cm^{-2} at 1.5 V),[21] $La_{0.6}Ca_{0.4}Fe_{0.8}Ni_{0.2}O_{3-\delta}$ (1.41A cm^{-2} at 2 V),[30] $La_{0.6}Sr_{0.4}Fe_{0.9}Mn_{0.1}O_{3-\delta}$ (1.107 A cm^{-2} at 2 V),[56] etc. under similar testing conditions. The comparable current density and R_p shown in single and symmetrical cells imply that LCCF64 has excellent catalytic activity for CO_2 electrolysis..

3.8 Stability Evaluation. Figure 9(a) shows the short-term stability of single cells with LCCF64 as the cathode at various constant applied currents. The output voltage remained stable at different levels as the applied current density increased from 0.3 to 1.5 A cm^{-2}. Meanwhile, the outlet gas was connected to a GC to moinitor CO production. The CO production rate and Faraday efficiency were calculated based on GC analysis and the Faraday law.[57] With the increase in the applied current density, CO production rate increases from 1.67 to 9.12 mL min^{-1} cm^{-2}, and the Faraday efficiency rises from 70.57% to 88.18% (Figure 9(b)). The highest Faraday efficiency achieved in this work was 88.18% at an applied current density of 1.2 A cm^{-2}, which is comparable to the reported cathodes in similar cell configurations for CO_2 electrolysis.[22,58,59]

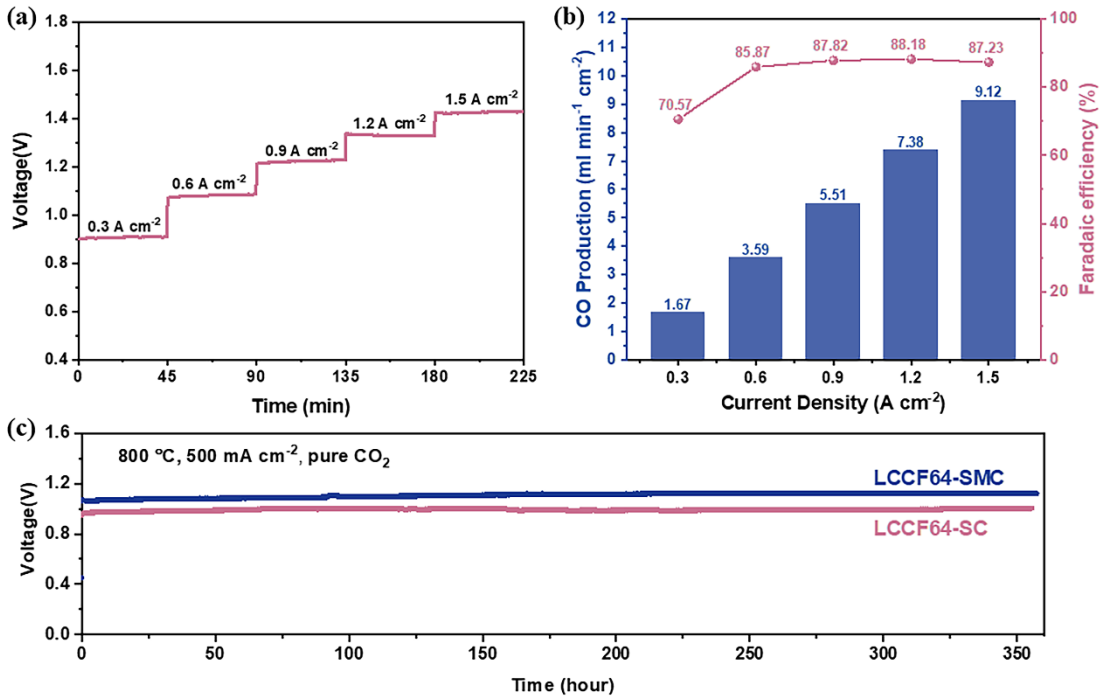

Figure 9. (a) Short-term stability, and (b) corresponding CO production rate and faradaic efficiency at various current density for CO_2 electrolysis in SOEC with LCCF64 as cathode at 800 °C; (c) Long-term stability of single cell (SC) and symmetrical cell (SMC) with LCCF64 as electrode.

The long-term stability of of the single and symmetrical cells with the LCCF64 cathode was assessed by measuring the cell output voltage under a constant current density of 0.5 A cm^{-2} at 800 °C for 350 hours. Figure 9(c) shows that the output voltage initially increased slightly and then stabilized, owing to Ca carbonation and then balance between the formation and decomposition of $CaCO_3$, as illustrated in eq. 3. After the long-term stability testing was completed, the electrode/electrolyte interface of the tested cell was examined using scanning electron microscopy (SEM), as depicted in Figure S4(b). Comparative analysis of the microstructure of the cell before testing (Figure S4(a)) revealed that, although the LCCF64 cathode exhibited slight agglomeration attributable to the observed phase change discussed in the previous XRD section, the interfacial region between the electrode and electrolyte demonstrated robust connectivity after a rigorous 350-hour stability test. This connectivity ensures seamless ion transportation across the electrode/electrolyte interface.[13] Consequently, the cell

exhibited a stable voltage output under a constant current load, exhibiting negligible signs of degradation.

4. CONCLUSIONS

In summary, LCxCF (x=0.2-0.6) perovskite was developed as cathode materials with in-situ exsolved Co/CoFe alloy nanoparticles embedded on perovskite backbone, and LCCF64 displayed the most homogeneous nanoparticles distribution. Excellent redox reversibility was demonstrated by TGA measurement, and high electrical conductivity in air and pure CO_2 was manifested using a four-probe DC method, offering LCxCF the necessary properties to serve as a suitable electrode in SOEC. In addition, LCCF64 showed the highest CO_2 adsorption ability due to the appropriate grain size and the increased oxygen vacancy generated from charge compensation. Moreover, the appearance of $Ca_2Fe_2O_5$ phase and the exsolved Co/CoFe alloy nanoparticles during CO_2 electrolysis further induced extra oxygen vacancy in LCCF64, resulting in a considerably high current density of 2.24 A cm^{-2} and 1.78 A cm^{-2} at 1.5 V for single and symmetrical SOECs at 800 °C, respectively. A high faradic efficiency of 88.18% and a high CO production rate of 9.12 ml^{-1} min^{-1} cm^{-2} were achieved at an applied current density of 1.2 A cm^{-2} at 800 °C for single cells using LCCF64 as the cathode for CO_2 electrolysis. Furthermore, the single and symmetrical cells using LCCF64 as the cathode exhibited good stability over 350 h CO_2 electrolysis test at constant current of 0.5 A cm^{-2} at 800 °C. This work points to a new direction toward developng electrodes with high peformance and stability for direct CO_2 electrolysis.

ACKNOWLEDGMENTS

Financial support from the U.S. National Science Foundation (1832809) and NASA EPSCoR (Grant # 80NSSC20M0233) is greatly appreciated. D.D. would like to thank the funding support by the U.S. Department of Energy (USDOE), Office of Energy Efficiency and Renewable Energy (EERE), Advanced Manufacturing Office (AMO) under DOE Idaho Operations Office under Contract No. DE-AC07-05ID14517.

ASSOCIATED CONTENT

Supporting Information

EIS plots for symmetrical cells with LCxCF (x=0.2-0.6) as electrode; I-V curves and Nyquist plots of the single cells with LCxCF (x= 0.2, 0.3, 0.5, 0.6) as cathode, and SEM images of the single cells before and after test.

Corresponding Authors

Dong Ding - *Energy & Environmental Science and Technology, Idaho National Laboratory, Idaho Falls, ID, 83401, USA*

Email: dong.ding@inl.gov

Fanglin Chen - *Department of Mechanical Engineering, University of South Carolina, Columbia, SC, 29208, USA*

Email: chenfa@cec.sc.edu

Author Contributions

The manuscript was written through the contributions of all authors. All authors have given approval to the final version of the manuscript.

Notes

The authors declare no competing financial interest.

REFERENCES

(1) Lu, J.; Chen, H.; Cai, X. From Global to National Scenarios: Exploring Carbon Emissions to 2050. *Energy Strateg. Rev.* **2022**, *41*, 100860.

(2) Yu, B.; Qiao, J.; Zhang, J.; Yu, S. B.; Zheng, Y.; Wang, J.; Zhang, W.; Chen, J. Featuring Work from the Research Groups of Associate Professor As Featured in: A Review of High Temperature Co-Electrolysis of H_2O and CO_2 to Produce Sustainable Fuels Using Solid Oxide Electrolysis Cells (SOECs): Advanced Materials and Technology. *Chem. Soc. Rev.* **2017**, *46*, 1427.

(3) Jiang, Y.; Chen, F.; Xia, C. A Review on Cathode Processes and Materials for Electro-Reduction of Carbon Dioxide in Solid Oxide Electrolysis Cells. *J. Power Sources* **2021**, *493*, 229713.

(4) Dong, D.; Xu, S.; Shao, X.; Hucker, L.; Marin, J.; Pham, T.; Xie, K.; Ye, Z.; Yang, P.; Yu, L.; Parkinson, G.; Li, C.-Z. Hierarchically Ordered Porous Ni-Based Cathode-Supported Solid Oxide Electrolysis Cells for Stable CO_2 Electrolysis without Safe Gas. *J. Mater. Chem. A* **2017**, *5* (5), 24098.

(5) Song, Y.; Zhou, Z.; Zhang, X.; Zhou, Y.; Gong, H.; Lv, H.; Liu, Q.; Wang, G.; Bao, X. Pure CO_2 Electrolysis over an Ni/YSZ Cathode in a Solid Oxide Electrolysis Cell. *J. Mater. Chem. A* **2018**, *6* (28), 13661–13667.

(6) Xu, S.; Li, S.; Yao, W.; Dong, D.; Xie, K. Direct Electrolysis of CO_2 Using an Oxygen-Ion Conducting Solid Oxide Electrolyzer Based on $La_{0.75}Sr_{0.25}Cr_{0.5}Mn_{0.5}O_{3-\delta}$ Electrode. *J. Power Sources* **2013**, *230*, 115–121.

(7) Ye, L.; Hu, X.; Wang, X.; Chen, F.; Tang, D.; Dong, D.; Xie, K. Enhanced CO_2 Electrolysis with a $SrTiO_3$ Cathode through a Dual Doping Strategy. *J. Mater. Chem.*

A **2019**, *7* (6), 2764-2772.

(8) Wu, M.; Zhou, X.; Xu, J.; Li, S.; Pan, L.; Zhang, N. Electrochemical Performance of $La_{0.3}Sr_{0.7}Ti_{0.3}Fe_{0.7}O_{3-\delta}/CeO_2$ Composite Cathode for CO_2 Reduction in Solid Oxide Electrolysis Cells. *J. Power Sources* **2020**, *451*, 227334.

(9) Deka, D. J.; Kim, J.; Gunduz, S.; Jain, D.; Shi, Y.; Miller, J. T.; Co, A. C.; Ozkan, U. S. Coke Formation during High-Temperature CO_2 Electrolysis over $AFeO_3$ (A = La/Sr) Cathode: Effect of A-Site Metal Segregation. *Appl. Catal. B Environ.* **2021**, *283*, 119642.

(10) Wang, W.; Li, H.; Regalado Vera, C. Y.; Lin, J.; Park, K.-Y.; Lee, T.; Ding, D.; Chen, F.; Improving the Performance for Direct Electrolysis of CO_2 in Solid Oxide Electrolysis Cells with a $Sr_{1.9}Fe_{1.5}Mo_{0.5}O_{6-\delta}$ Electrode via Infiltration of Pr_6O_{11} Nanoparticles. *J. Mater. Chem. A* **2023**, *11* (16), 9039–9048.

(11) Zhang, S.; Jiang, Y.; Han, H.; Li, Y.; Xia, C. Perovskite Oxyfluoride Ceramic with In Situ Exsolved Ni−Fe Nanoparticles for Direct CO_2 Electrolysis in Solid Oxide Electrolysis Cells. *ACS Appl. Mater. Interfaces* **2022**, *14* (25), 28854–28864.

(12) Liu, C.; Sun, C.; Bian, L.; Yu, W.; Qi, J.; Li, S.; Gao, J.; Peng, J.; Peng, J.; An, S. Robust Ni-Doped Ruddlesden-Popper $(La,Sr)Fe_{1-x}Ni_xO_{4+\delta}$ Oxide as Solid Oxide Cells Fuel Electrode for CO_2 Electrolysis. *Int. J. Hydrogen Energy* **2022**, *47* (16), 9517–9526.

(13) Liu, C.; Li, S.; Gao, J.; Bian, L.; Hou, Y.; Wang, L.; Peng, J.; Bao, J.; Song, X.; An, S. Enhancing CO_2 Catalytic Adsorption on an Fe Nanoparticle-Decorated $LaSrFeO_{4+\delta}$ Cathode for CO_2 Electrolysis. *ACS Appl. Mater. Interfaces* **2021**, *13*, 8238.

(14) Hu, S.; Zhang, L.; Liu, H.; Li, W.; Cao, Z.; Cai, L.; Zhu, Y.; Zhu, X.; Yang, W.

Detrimental Phase Evolution Triggered by Ni in Perovskite-Type Cathodes for CO_2 Electroreduction. *J. Energy Chem.* **2019**, *36*, 87–94.

(15) Kamecki, B.; Cempura, G.; Jasiński, P. J.; Wang, S.-F.; Molin, S. Tuning Electrochemical Performance by Microstructural Optimization of the Nanocrystalline Functional Oxygen Electrode Layer for Solid Oxide Cells. *ACS Appl. Mater. Interfaces* **2022**, *14*, 57449–57459.

(16) Feng, W.; Liu, T.; Li, R.; Song, Y.; Wang, G.; Bao, X. Optimizing the Electronic Structures of $Ca_xSr_{1-x}Co_{0.7}Fe_{0.3}O_{3-\delta}$ Anodes for High-Temperature Oxygen Evolution Reaction. *Chem. Catal***. 2023**, *3* (3), 100504.

(17) Rostaghi Chalaki, H.; Babaei, A.; Ataie, A.; Seyed-Vakili, S. V. $LaFe_{0.6}Co_{0.4}O_3$ Promoted LSCM/YSZ Anode for Direct Utilization of Methanol in Solid Oxide Fuel Cells. *Ionics* **2020**, *26*, 1011–1018.

(18) Song, J.; Ning, D.; Bouwmeester, H. J. M. Influence of Alkaline-Earth Metal Substitution on Structure, Electrical Conductivity and Oxygen Transport Properties of Perovskite-Type Oxides $La_{0.6}A_{0.4}FeO_{3-\delta}$ (A = Ca, Sr and Ba). *Phys. Chem. Chem. Phys.* **2020**, *22* (21), 11984–11995.

(19) Teraoka, Y.; Nobunaga, T.; Yamazoe, N. Effect of Cation Substitution on the Oxygen Semipermeability of Perovskite-Type Oxides. *Chem. Lett.* **1988**, *17* (3), 503–506.

(20) Li, S.; Jin, W.; Xu, N.; Shi, J. Oxygen Vacancy Concentration Variation, Diffusivity and Thermo-Chemical Stability of $La_{0.2}Ba_{0.8}Co_{0.2}Fe_{0.8}O_{3-\delta}$ Membranes. *J. Mater. Sci.* **2000**, *35* (17), 4329–4335.

(21) Yang, Z.; Ma, C.; Wang, N.; Jin, X.; Jin, C.; Peng, S. Electrochemical Reduction

of CO_2 in a Symmetrical Solid Oxide Electrolysis Cell with $La_{0.4}Sr_{0.6}Co_{0.2}Fe_{0.7}Nb_{0.1}O_{3-\delta}$ electrode. *J. CO_2 Util.* **2019**, *33*, 445–451.

(22) Liu, S.; Liu, Q.; Luo, J.-L. CO_2-to-CO Conversion on Layered Perovskite with in Situ Exsolved Co-Fe Alloy Nanoparticles: An Active and Stable Cathode for Solid Oxide Electrolysis Cells. *J. Mater. Chem. A* **2016**, *4* (44), 17521–17528.

(23) Hou, Y.; Wang, Y.; Wang, L.; Zhang, Q.; Chou, K. C. Electrochemical Properties of $La_{0.5}Sr_{0.5}Fe_{0.95}Mo_{0.05}O_{3-\delta}$ as Cathode Materials for IT-SOEC. *RSC Adv.* **2021**, *11* (51), 32077–32084.

(24) Tian, Y.; Zheng, H.; Zhang, L.; Chi, B.; Pu, J.; Li, J. Direct Electrolysis of CO_2 in Symmetrical Solid Oxide Electrolysis Cell based on $La_{0.6}Sr_{0.4}Fe_{0.8}Ni_{0.2}O_{3-\delta}$ Electrode. *J. Electrochem. Soc***.** **2018**, *165* (2), F17.

(25) Su, M.; Huan, D.; Hu, X.; Zhu, K.; Peng, R.; Xia, C. Understanding the Favorable CO_2 Tolerance of Ca-Doped $LaFeO_3$ Perovskite Cathode for Solid Oxide Fuel Cells. *J. Power Sources* **2022**, *521* (96), 230907.

(26) Tian, Y.; He, S.; Liu, Y.; Yang, C.; Yang, R.; Li, Y.; Wang, X.; Li, W. L.; Chi, B.; Pu, J. Comprehensive Understanding of Alkaline-Earth Elements Effects on Electrocatalytic Activity and Stability of $LaFe_{0.8}Ni_{0.2}O_3$ Electrode for High-Temperature CO_2 Electrolysis. *J. CO_2 Util.* **2021**, *53*, 101727.

(27) Choi, S.; Park, S.; Shin, J.; Kim, G. The Effect of Calcium Doping on the Improvement of Performance and Durability in a Layered Perovskite Cathode for Intermediate-Temperature Solid Oxide Fuel Cells. *J. Mater. Chem. A* **2015**, *3* (11), 6088–6095.

(28) Ortiz-Vitoriano, N.; De Larramendi, I. R.; Cook, S. N.; Burriel, M.; Aguadero,

A.; Kilner, J. A.; Rojo, T. The Formation of Performance Enhancing Pseudo-Composites in the Highly Active $La_{1-X}Ca_xFe_{0.8}Ni_{0.2}O_3$ System for IT-SOFC Application. *Adv. Funct. Mater.* **2013**, *23* (41), 5131–5139.

(29) Li, Y.; Li, Y.; Yu, L.; Hu, Q.; Wang, Q.; Maliutina, K.; Fan, L. Achieving Excellent and Durable CO_2 Electrolysis Performance on a Dual-Phase Fuel Electrode in Solid Oxide Electrolysis Cells. *J. Power Sources* **2021**, *491*, 229599.

(30) Tian, Y.; Zhang, L.; Liu, Y.; Jia, L.; Yang, J.; Chi, B.; Pu, J.; Li, J. A Self-Recovering Robust Electrode for Highly Efficient CO_2 Electrolysis in Symmetrical Solid Oxide Electrolysis Cells. *J. Mater. Chem. A* **2019**, *7* (11), 6395–6400.

(31) Qian, B.; Liu, C.; Wang, S.; Yin, B.; Zheng, Y.; Ge, L.; Chen, H.; Zhang, C. Ca-Doped $La_{0.75}Sr_{0.25}Cr_{0.5}Mn_{0.5}O_3$ Cathode with Enhanced CO_2 Electrocatalytic Performance for High-Temperature Solid Oxide Electrolysis Cells. *Int. J. Hydrogen Energy* **2021**, *46* (67), 33349–33359.

(32) Li, H.; Wang, W.; Lin, J.; Park, K.-Y.; Lee, T.; Heyden, A.; Ding, D.; Chen, F. Improved Cell Performance and Sulphur Tolerance Using A-Site Substituted $Sr_2Fe_{1.4}Ni_{0.1}Mo_{0.5}O_{6-\delta}$ Anodes for Solid-Oxide Fuel Cells. *Clean Energy* **2023**, *7* (1), 70–83.

(33) Pidburtnyi, M.; Zanca, B.; Coppex, C.; Jimenez-Villegas, S.; Thangadurai, V. A Review on Perovskite-Type $LaFeO_3$ Based Electrodes for CO_2 Reduction in Solid Oxide Electrolysis Cells: Current Understanding of Structure−Functional Property Relationships. *Chem. Mater.* **2021**, *33*, 4268.

(34) Guo, H.; Feng, J.; Zhao, Y.; Wang, S.; Ma, X. Effect of Micro-Structure and Oxygen Vacancy on the Stability of (Zr-Ce)-Additive CaO-Based Sorbent in CO_2

Adsorption. *J. CO_2 Util.* **2017**, *19*, 165–176.

(35) Mori, M.; Hiei, Y.; Sammes, N. M. Sintering Behavior and Mechanism of Sr-Doped Lanthanum Chromites with A Site Excess Composition in Air. *Solid State Ionics* **1999**, *123* (1), 103–111.

(36) Lv, H.; Zhou, Y.; Zhang, X.; Song, Y.; Liu, Q.; Wang, G.; Bao, X. Infiltration of $Ce_{0.8}Gd_{0.2}O_{1.9}$ Nanoparticles on $Sr_2Fe_{1.5}Mo_{0.5}O_{6-\delta}$ Cathode for CO_2 Electroreduction in Solid Oxide Electrolysis Cell. *J. Energy Chem.* **2019**, *35*, 71–78.

(37) Ansari, H. M.; Addo, P. K.; Mulmi, S.; Yuan, H.; Botton, G. A.; Thangadurai, V.; Birss, V. I. Deciphering the Interaction of Single-Phase $La_{0.3}Sr_{0.7}Fe_{0.7}Cr_{0.3}O_{3-\delta}$ with CO_2/CO Environments for Application in Reversible Solid Oxide Cells. *ACS Appl. Mater. Interfaces* **2022**, *14* (11), 13388–13399.

(38) Xu, C.; Sun, K.; Yang, X.; Ma, M.; Ren, R.; Qiao, J.; Wang, Z.; Zhen, S.; Sun, W. Highly Active and CO_2-Tolerant $Sr_2Fe_{1.3}Ga_{0.2}Mo_{0.5}O_{6-\delta}$ Cathode for Intermediate-Temperature Solid Oxide Fuel Cells. *J. Power Sources* **2020**, *450*, 227722.

(39) Li, Y.; Li, Y.; Zhang, S.; Ren, C.; Jing, Y.; Cheng, F.; Wu, Q.; Lund, P.; Fan, L. Mutual Conversion of CO-CO_2 on a Perovskite Fuel Electrode with Endogenous Alloy Nanoparticles for Reversible Solid Oxide Cells. *ACS Appl. Mater. Interfaces* **2022**, *14* (7), 9138–9150.

(40) Xie, L.; Liang, J.; Priest, C.; Tanyuan Wang, bc; Ding, D.; Wu, G.; Li, Q. Engineering the Atomic Arrangement of Bimetallic Catalysts for Electrochemical CO_2 Reduction. *ChemComm*, **2021**, *57* (15), 1839–1854.

(41) Yang, X.; Sun, W.; Ma, M.; Xu, C.; Ren, R.; Qiao, J.; Wang, Z.; Li, Z.; Zhen, S.; Sun, K. Achieving Highly Efficient Carbon Dioxide Electrolysis by in Situ

Construction of the Heterostructure. *ACS Appl. Mater. Interfaces* **2021**, *13* (17), 20060–20069.

(42) Zhang, L.; Sun, W.; Xu, C.; Ren, R.; Yang, X.; Qiao, J.; Wang, Z.; Zhen, S.; Sun, K. Two-Fold Improvement in Chemical Adsorption Ability to Achieve Effective Carbon Dioxide Electrolysis. *Appl. Catal. B Environ.* **2022**, *317*, 121754.

(43) Li, H.; Jiao, X.; Li, L.; Zhao, N.; Xiao, F.; Wei, W.; Sund, Y.; Zhang, B.; Synthesis of Glycerol Carbonate by Direct Carbonylation of Glycerol with CO_2 over Solid Catalysts Derived from Zn/Al/La and Zn/Al/La/M (M= Li, Mg and Zr) Hydrotalcites[J]. *Catal. Sci. Technol*. **2015**, *5* (2), 989–1005.

(44) Zhou, Y.; Zhou, Z.; Song, Y.; Zhang, X.; Guan, F.; Lv, H.; Liu, Q.; Miao, S.; Wang, G.; Bao, X. Enhancing CO_2 Electrolysis Performance with Vanadium-Doped Perovskite Cathode in Solid Oxide Electrolysis Cell. *Nano Energy* **2018**, *50*, 43–51.

(45) Benali, A.; Souissi, A.; Bejar, M.; Dhahri, E.; Graça, M. F. P.; Valente, M. A. Dielectric Properties and Alternating Current Conductivity of Sol-Gel Made $La_{0.8}Ca_{0.2}FeO_3$ Compound. *Chem. Phys. Lett.* **2015**, *637*, 7–12.

(46) Dhankhar, S.; Bhalerao, G.; Baskar, K. Synthesis and Characterization of Polycrystalline Brownmillerite Cobalt Doped $Ca_2Fe_2O_5$. *AIP Publishing LLC*, **2016**, *1731*, 140032.

(47) Cascos, V.; Martínez-Coronado, R.; Alonso, J. A.; Fernández-Díaz, M. T. Structural and Electrical Characterization of the Co-Doped $Ca_2Fe_2O_5$ Brownmillerite: Evaluation as SOFC-Cathode Materials. *Int. J. Hydrogen Energy* **2015**, *40* (15), 5456–5468.

(48) Qi, H.; Thomas, T.; Li, W.; Li, W.; Xia, F.; Zhang, N.; Sabolsky, E. M.; Zondlo,

J.; Hart, R.; Liu, X. Reduced Thermal Expansion and Enhanced Redox Reversibility of $La_{0.5}Sr_{1.5}Fe_{1.5}Mo_{0.5}O_{6-\delta}$ Anode Material for Solid Oxide Fuel Cells. *ACS Appl. Energy Mater.* **2019**, *2* (6), 4244–4254.

(49) Xia, C.; Peng, R.; Huan, D.; Zhang, L.; Zhang, S.; Shi, N.; Li, X.; Zhu, K.; Lu, Y. Ruddlesden-Popper Oxide $SrEu_2Fe_2O_7$ as a Promising Symmetrical Electrode for Pure CO_2 Electrolysis. *J. Mater. Chem. A* **2021**, 9 (5), 2706–2713.

(50) Bebelis, S.; Kotsionopoulos, N.; Mai, A.; Tietz, F. Electrochemical Characterization of Perovskite-Based SOFC Cathodes. *J. Appl. Electrochem.* **2006**, *37* (1), 15–20.

(51) Cao, Z.; Wei, B.; Miao, J.; Wang, Z.; Lü, Z.; Li, W.; Zhang, Y.; Huang, X.; Zhu, X.; Feng, Q.; Sui, Y. Efficient Electrolysis of CO_2 in Symmetrical Solid Oxide Electrolysis Cell with Highly Active $La_{0.3}Sr_{0.7}Fe_{0.7}Ti_{0.3}O_3$ Electrode Material. *Electrochem. commun.* **2016**, *69*, 80–83.

(52) Tao, G.; Sridhar, K. R.; Chan, C. L. Study of Carbon Dioxide Electrolysis at Electrode/Electrolyte Interface: Part I. Pt/YSZ Interface. *Solid State Ionics* **2004**, *175* (1–4), 615–619.

(53) Molero-Sánchez, B.; Addo, P.; Buyukaksoy, A.; Paulson, S.; Birss, V. Electrochemistry of $La_{0.3}Sr_{0.7}Fe_{0.7}Cr_{0.3}O_{3-\delta}$ as an Oxygen and Fuel Electrode for RSOFCs. *Faraday Discuss.* **2015**, *182*, 159–175.

(54) Yang, Y.; Li, Y.; Jiang, Y.; Zheng, M.; Hong, T.; Wu, X.; Xia, C. The Electrochemical Performance and CO_2 Reduction Mechanism on Strontium Doped Lanthanum Ferrite Fuel Electrode in Solid Oxide Electrolysis Cell. *Electrochim. Acta* **2018**, *284*, 159–167.

(55) Wang, S.; Jiang, H.; Gu, Y.; Yin, B.; Chen, S.; Shen, M.; Zheng, Y.; Ge, L.; Chen, H.; Guo, L. Mo-Doped $La_{0.6}Sr_{0.4}FeO_{3-\delta}$ as an Efficient Fuel Electrode for Direct Electrolysis of CO_2 in Solid Oxide Electrolysis Cells. *Electrochim. Acta* **2020**, *337*, 135794.

(56) Peng, X.; Tian, Y.; Liu, Y.; Wang, W.; Jia, L.; Pu, J.; Chi, B.; Li, J. An Efficient Symmetrical Solid Oxide Electrolysis Cell with LSFM-Based Electrodes for Direct Electrolysis of Pure CO_2. *J. CO_2 Util.* **2020**, *36*, 18–24.

(57) Liu, L.; Zhou, X.; Wang, Y.; Li, S.; Yin, R.; Guo, P.; Zhao, J.; Zhao, X.; Li, B. Composite Ceramic Cathode $La_{0.9}Ca_{0.1}Fe_{0.9}Nb_{0.1}O_{3-\delta}/Sc_{0.2}Zr_{0.8}O_{2-\delta}$ towards Efficient Carbon Dioxide Electrolysis in Zirconia-Based High Temperature Electrolyser. *Int. J. Hydrogen Energy* **2017**, *42* (22), 14905–14915.

(58) Ding, S.; Li, M.; Pang, W.; Hua, B.; Duan, N.; Zhang, Y. Q.; Zhang, S. N.; Jin, Z.; Luo, J. L. A-Site Deficient Perovskite with Nano-Socketed Ni-Fe Alloy Particles as Highly Active and Durable Catalyst for High-Temperature CO_2 Electrolysis. *Electrochim. Acta* **2020**, *335*, 135683.

(59) Park, S.; Kim, Y.; Han, H.; Chung, Y. S.; Yoon, W.; Choi, J.; Kim, W. B. In Situ Exsolved Co Nanoparticles on Ruddlesden-Popper Material as Highly Active Catalyst for CO_2 Electrolysis to CO. *Appl. Catal. B Environ.* **2019**, *248*, 147–156.

Table of Contents (TOC) graphic

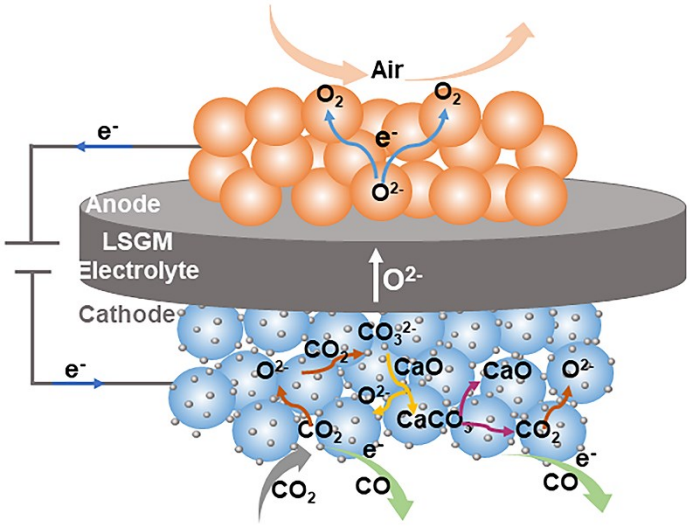

(1) CO_2 (g) $\rightarrow$ CO_2 (ads)

(2) $2CO_2$ (ads) + $2e^- \rightarrow 2CO + O^{2-}$

(3) CO_2 (ads) + $O^{2-} \rightarrow CO_3^{2-}$

(4) CO_3^{2-} + CaO $\rightarrow$ $CaCO_3$ + O^{2-}

(5) $CaCO_3 \leftrightarrow CaO + CO_2$

(6) $2O^{2-} - 4e^- \rightarrow O_2$ (g)